Electronic Supplementary Material (ESI) for Energy & Environmental Science.
This journal is © The Royal Society of Chemistry 2020

Supporting Information

Visualizing morphological principles for efficient photocurrent generation in organic non-fullerene acceptor blends

Wolfgang Köntges, Pavlo Perkhun, Jochen Kammerer, Riva Alkarsifi, Uli Würfel, Olivier Margeat, Christine Videlot-Ackermann, Jean-Jacques Simon, Rasmus R. Schröder, Jörg Ackermann, Martin Pfannmöller

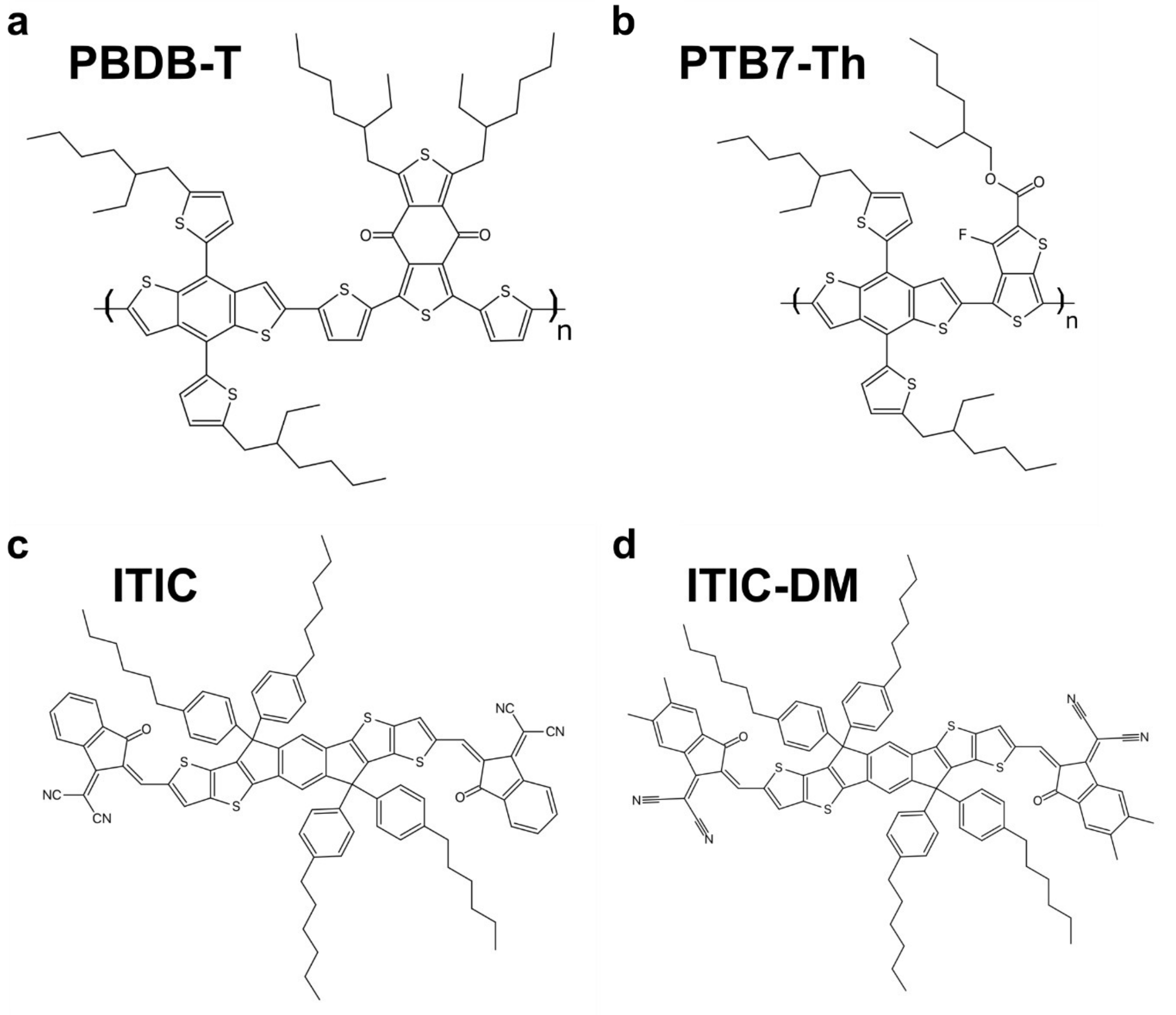

Fig. S1 Chemical structures of organic materials studied in this work. a, Full name: Poly[(2,6-(4,8-bis(5-(2-ethylhexyl)thiophen-2-yl)-benzo[1,2-b:4,5-b’]dithiophene))-alt-(5,5-(1’,3’-di-2-thienyl-5’,7’-bis(2-ethylhexyl)benzo[1’,2’-c:4’,5’-c’]dithiophene-4,8-dione)]. Chemical formula: $(C_{68}H_{78}O_2S_8)_n$ (**PBDB-T**). **b**, Full name: Poly[4,8-bis(5-(2-ethylhexyl)thiophen-2-yl)benzo[1,2-b;4,5-b']dithiophene-2,6-diyl-alt-(4-(2-ethylhexyl)-3-fluorothieno[3,4-b]thiophene-)-2-carboxylate-2-6-diyl)]. Chemical formula: $(C_{49}H_{57}FO_2S_6)_n$ (**PTB7-Th**). **c**, Full name: 3,9-bis(2-methylene-(3-(1,1-dicyanomethylene)-indanone))-5,5,11,11-tetrakis(4-hexylphenyl)-dithieno[2,3-d:2’,3’-d’]-s-indaceno[1,2-b:5,6-b’]dithiophene. Chemical formula: $C_{94}H_{82}N_4O_2S_4$ (**ITIC**). **d**, Full name: 3,9-bis(2-methylene-((3-(1,1-dicyanomethylene)-6,7-dimethyl)-indanone))-5,5,11,11-tetrakis(4-hexylphenyl)-dithieno[2,3-d:2’,3’-d’]-s-indaceno[1,2-b:5,6-b’]dithiophene. Chemical formula: $C_{98}H_{90}N_4O_2S_4$ (**ITIC-DM**).

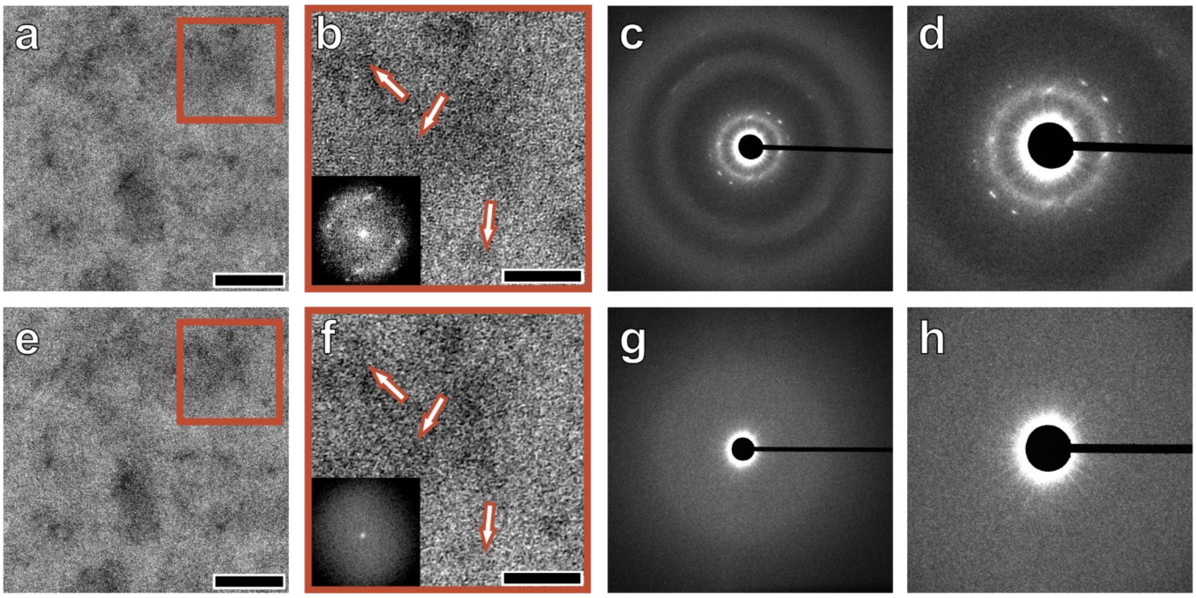

Fig. S2 Bright-field TEM images and electron diffraction (ED) patterns of a pure 30 nm thin ITIC film. **a**, First conventional TEM image indicating the area magnified in (**b**). Scalebar represents 100 nm. **b**, Magnified area indicated in (**a**) with the inserted power spectrum of this area. The arrows mark regions of ITIC crystallites. Scalebar represents 40 nm. **c**, ED pattern of another sample area. **d**, Magnified centre region of the ED pattern in (**c**). **e-h**, Bright-field TEM images and ED patterns at the same sample position as for the according images in (**a-d**) showing that the crystalline structures vanish by irradiation damage. Crystalline structures depend on intact end groups and side chains of the molecules[1]. Regarding the chemical structures of the organic materials in Fig. 1 it is reasonable to assume that certain carbon bonds are not regenerative after breaks by primary electrons. Hence, side chains and end groups are removed through the interaction with transmitting electrons in the TEM thereby influencing the electronic structure and thus, the low-energy loss signal. Furthermore, this leads to chemical distortions[2]. However, the π-σ-systems in the small molecule backbones and the repeating units of the polymers appear to be resistant against change of energy-loss signal. This is supported by Fig. 4 and 6 showing a stable π-σ plasmon signal between 10 eV and 40 eV for all materials after applying a dose of more than 150,000 electrons per nm².

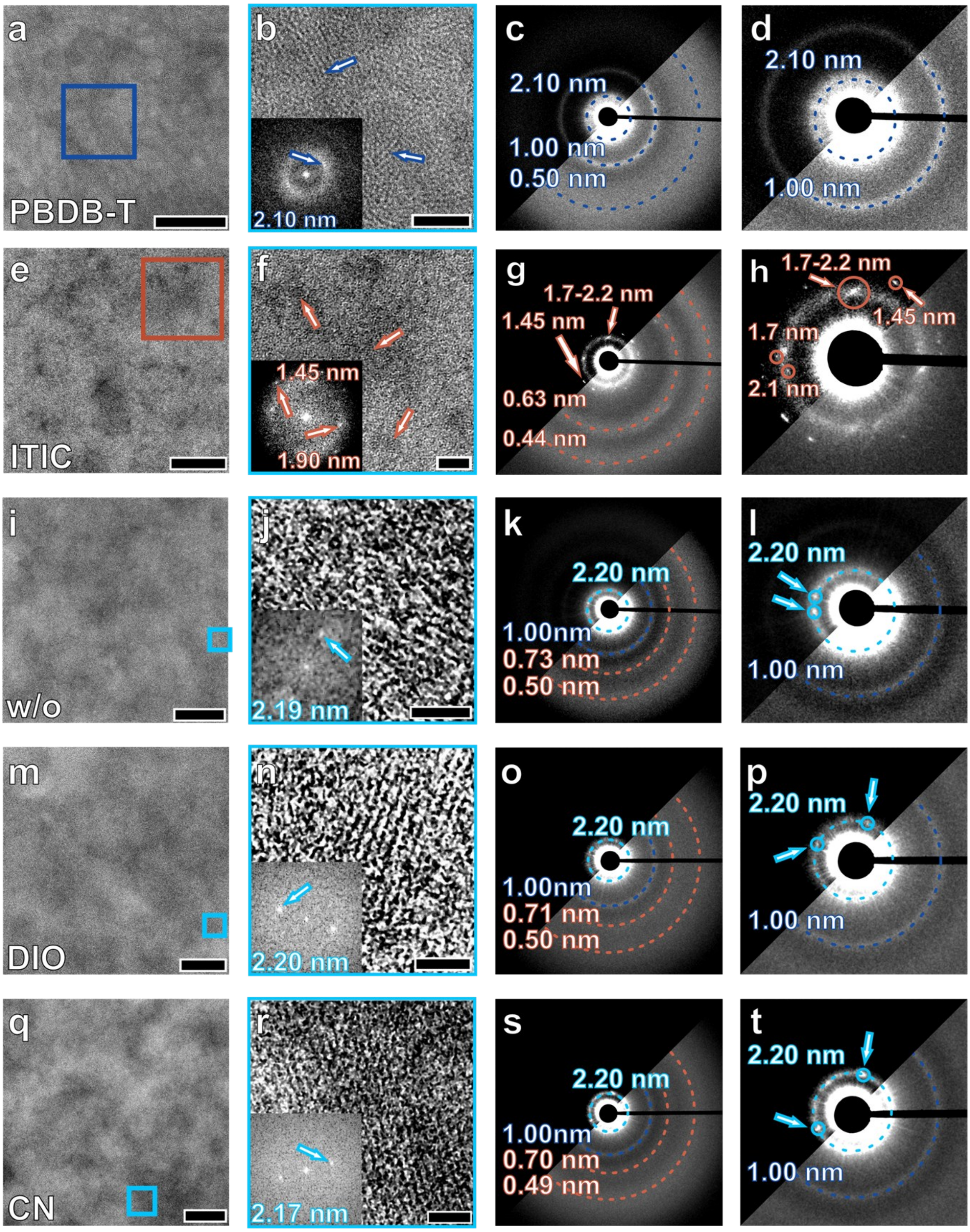

Fig. S3 Bright-field TEM images and electron diffraction (ED) patterns of pure PBDB-T, ITIC and blends of both materials. a-d, Thin layer of pure PBDB-T. **e-h**, Thin layer of pure ITIC (see also Fig. 2 in the main text). **i-l**, Blend processed without solvent additive. **m-p**, Blend processed with DIO. **q-t**, Blend processed with CN. All blends were post-annealed after spin coating. An exact description can be found in the main text and methods section. Scalebars in the first column represent 100 nm, in (**b**) and (**f**) 20 nm and in (**j**), (**n**) and (**r**) 10 nm.

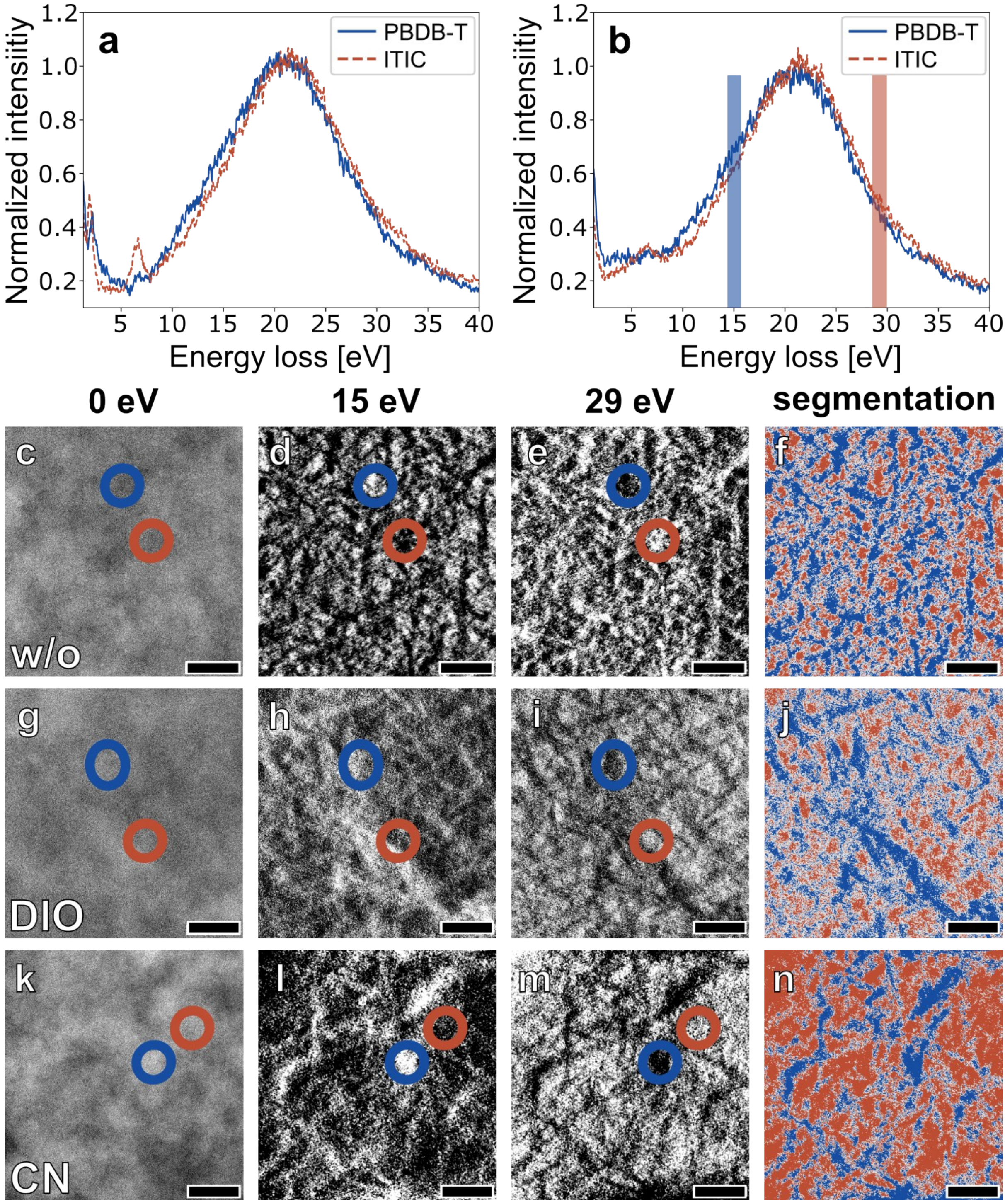

Fig. S4 TEM/ATAM analysis of 30 nm thin PBDB-T:ITIC blends processed with additional thermal annealing. **a**, Spectra of pure 30 nm thin PBDB-T and ITIC layers acquired by electron energy-loss spectroscopy (EELS). **b**, Spectra of pure 30 nm thin PBDB-T and ITIC layers acquired by EELS at the same sample position as in (**a**) after an electron dose of 150,000 electrons per nm^2. Here, the EELS signal below 10 eV is altered. However, the plasmon signal from 10-40 eV remains stable for even higher electron doses and can be utilized for ESI. A detailed discussion of irradiation damage can be found in Fig. 3. The coloured rectangles at energy-loss values of 15 eV and 29 eV indicate the energies for the inelastic images in the second and third column acquired by electron spectroscopic imaging (ESI). **c-n**, Bright-field TEM images (first column), ESI images (second and third column) and material distribution maps obtained by processing and analysis ESI image series (fourth column) of the blend layers. **c-f**, PBDB-T:ITIC layer processed without solvent additive. **g-j**, PBDB-T:ITIC layer processed with

DIO. **k-n**, PBDB-T:ITIC layer processed with CN. All layers were processed with additional thermal annealing at 140 °C for 15 min after spin coating. Scalebars represent 100 nm. Blue and brown circles in the first three columns mark regions corresponding to donor and acceptor phases, showing inverted contrast between blue and brown areas but similar signal in the bright-field TEM image in the first column. Hence, the contrast in the ESI images does not arise from thickness and density, i.e. mass-density differences.

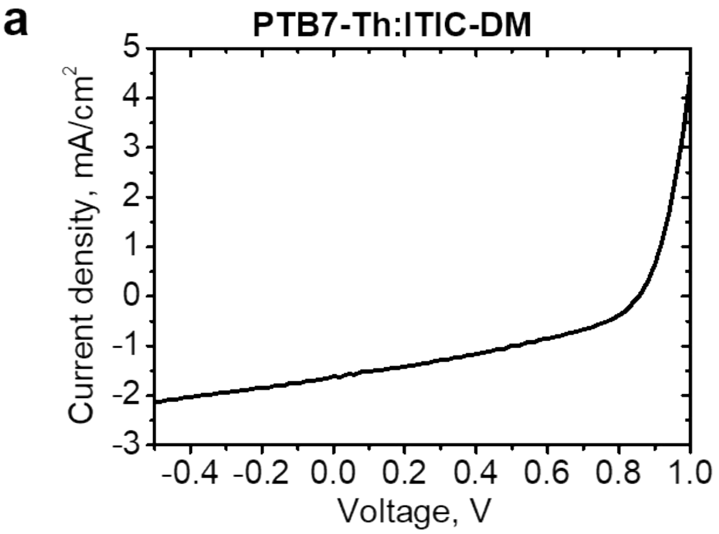

Voc, V	Jsc, mA	FF	PCEmax, %	PCEavg, % (# of cells)
0.85	1.6	38.29	0.52	0.44 (± 0.02) (6)

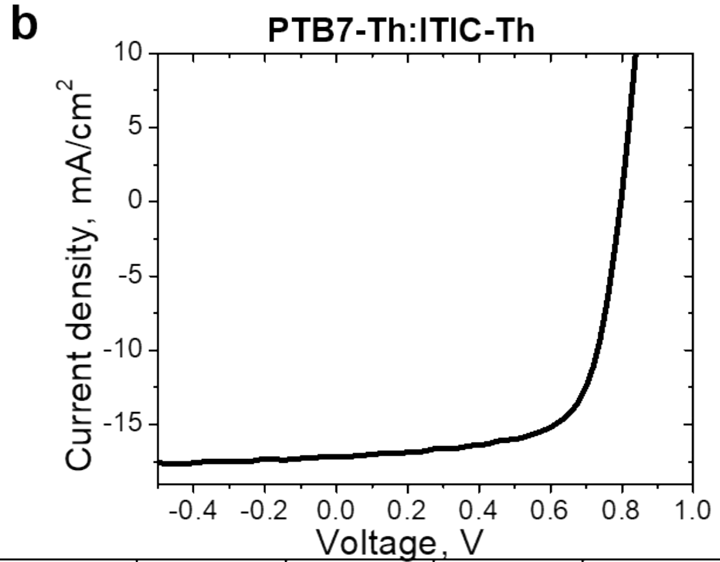

Voc, V	Jsc, mA	FF	PCEmax, %	PCEavg, % (# of cells)
0.8	17.15	67.78	9.30	8.918 (±0.12) (5)

Fig. S5 J-V curves and photovoltaic parameters of fabricated PTB7-Th:ITIC-DM (a) and PTB7-Th:ITIC-Th (b) solar cells. Preparation of the PTB7-Th:ITIC-Th cell followed a protocol different from the other cells discussed in the work at hand: The solar cells were manufactured with an inverted architecture: glass/ITO/ZnO/PTB7-Th:ITIC-Th/MoO3/Ag. First ITO substrates were thoroughly cleaned by sonication in acetone and ethanol followed by rinsing with water and sonication in isopropanol for 10 min in each solvent and applying ultraviolet-ozone for 15 min at 80 °C. A thin layer of 2.5% wt. solution of ZnO in isopropanol (Avantama) was spin-coated on the cleaned ITO precoated glass substrate in the ambient conditions at a speed of 5000 rpm for 60 s followed by heating on a hot-plate at 120 °C for 10 min. The blend solution of PTB7-Th:ITIC-Th in chlorobenzene with concentration of 20 mg/mL was prepared by stirring at 60° C overnight. 3% wt .of chloronaphtalene was added to the ink after 1 hour of mixing. The PTB7-Th:ITIC-Th layers were spin-coated inside of argon-filled glow-box on top of the ZnO at 800 rpm with the following annealing at 80 °C for 5 min. In order to complete devices, 2 nm of MoO3 and 100 nm of Ag were thermally evaporated at 1 × 10^{-7} mbar through a shadow mask to obtain a device area of 0.27 cm^2.

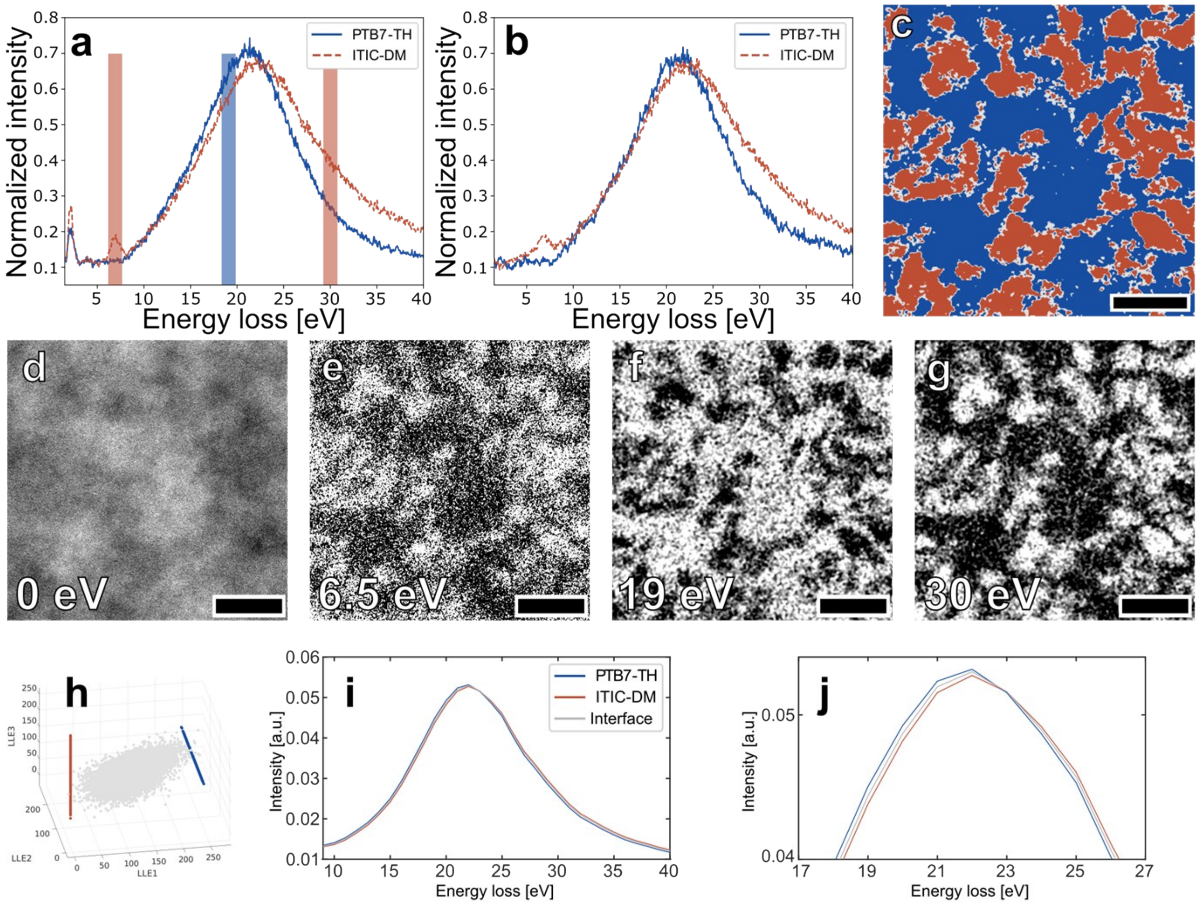

Fig. S6 TEM/ATAM analysis of a 20 nm thin PTB7-Th:ITIC-DM blend. **a**, EEL spectra of pure 20 nm thin PTB7-TH and ITIC-DM layers. The coloured rectangles at energy-loss values of 6.5, 19, and 30 eV indicate the energies for the inelastic images in (**e-g**) acquired by ESI. **b**, Spectra of pure 20 nm thin PTB7-TH and ITIC-DM layers acquired by EELS at the same sample position as in (**a**) but after an electron dose of 150,000 electrons per nm². Similar structural changes and stabilities as for PBDB-T:ITIC as in Fig. 4 are observed. **c**, Material distribution map obtain from a series of ESI images including those in (**f**) and (**g**) through the machine learning approach discussed in the main text and methods section. **d**, Bright-field TEM image. **e-g**, ESI images as indicated at energy windows marked in the EELS spectra in (**a**). The image in (**e**) shows the same contrast as in (**g**) with a lower signal to noise ratio. The image in (**f**) shows an inverted contrast to (**e**) and (**g**) corresponding to the signal differences in the EEL spectra in (**a**) at the indicated energy values. **h**, Scatterplot with axes directions spanned by the first three dimensions from locally linear embedding showing three distinct clusters (two pure for donor and acceptor domains and one mixed), from which the segmentation of the material distribution map in (**c**) was deduced. Each point in the scatterplot corresponds to one ESI spectrum from the spatially resolved analytical data set but represented in three-dimensional space that retains the local structure and specific underlying spectral differences. **i**, ESI spectra calculated from the ESI images by averaging over all pixels of the corresponding material phase. **j**, Magnified region of the average spectra in (**j**). Scalebars represent 100 nm.

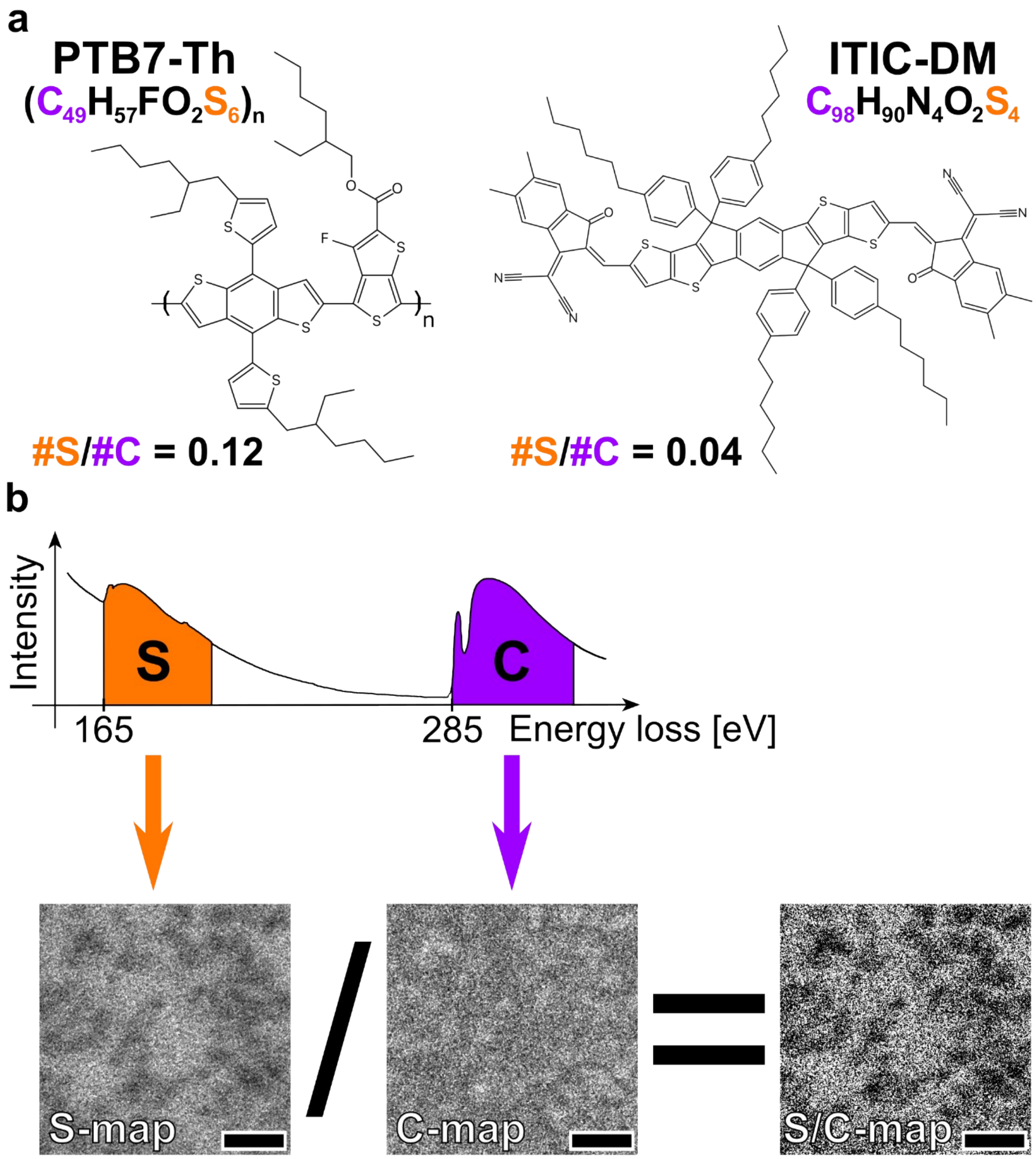

Fig. S7 Detailed illustration of acquisition and calculation of the S/C ratio map of the same sample position as shown in Fig. 6d-g. a, Chemical structures and formulas of PTB7-Th and ITIC-DM and calculation of the sulphur to carbon ratio for both materials. For PTB7-Th the calculation was performed for the repeating unit of the polymer. **b**, Schematic illustration of the electron energy loss spectrum at the sulphur L-ionization edge and carbon K-ionization edge. The elemental maps for both materials were acquired by the three-window method for background removal[3]. The sulphur carbon ratio (S/C) map was calculated by dividing the sulphur by the carbon map. Scalebars represent 100 nm. The contrast in the S/C map is the same as in Fig. 6f, but the signal to noise ratio is too low for a machine learning based material segmentation. This is only feasible with an ESI image series from 10-40 eV.

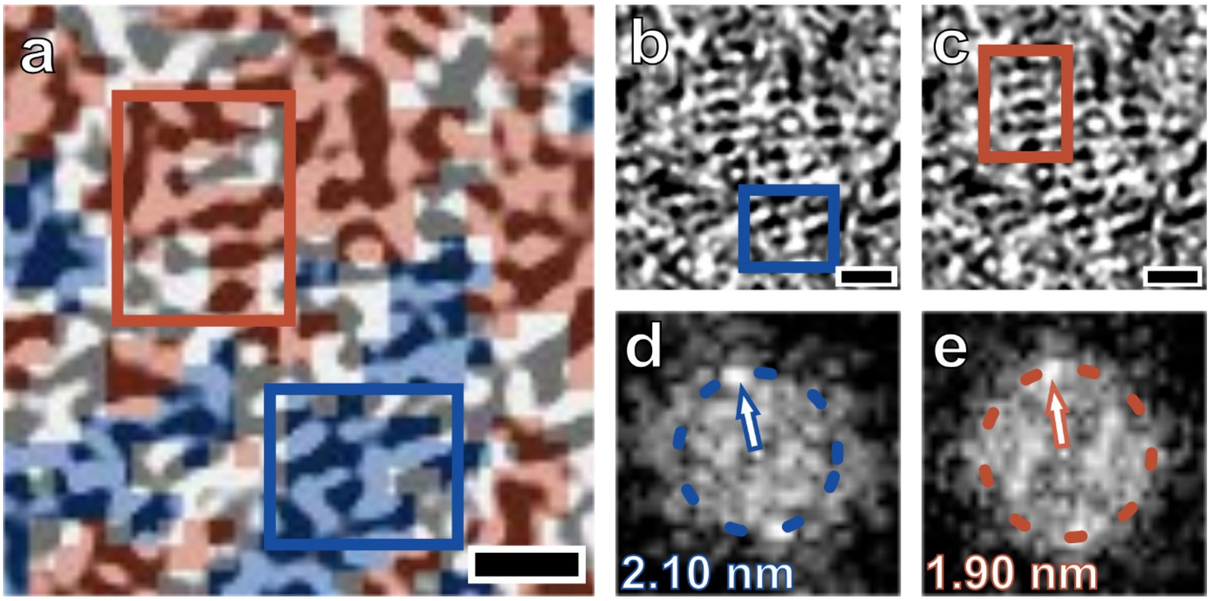

Fig. S8 Precise analysis of crystalline subareas in Fig. 3d. a, Correlative overlay of a bright-field TEM image and an ATEM material distribution map shown in Fig. 3d. **b-c,** Bright-field TEM image from the selected areas in (**a**) with smaller rectangles to mark donor and acceptor crystals assigned by ATEM. **d-e**, Corresponding power spectra of the donor and acceptor regions marked in (**b**) and (**c**). Scalebars represent 5 nm.

The correlation of intermediate-resolution information and material phase assignment as shown in Fig. S8 is done at the nanometer scale. The location of fringes is directly translated in locations of ordered molecules, which is only possible when the delocalisation induced by the TEM imaging system is small enough. Delocalisation is influenced by several parameters given in Eq. S1. They include the electron wavelength, the defocus of the objective lens, the spatial frequency that in this case corresponds to a spacing of ca. 2 nm and the spherical aberration. The spherical aberration could be reduced to what is considered a low value using an aberration corrector in the used microscope. Furthermore, images were recorded near focus so that -50 nm can be regarded as maximum value of underfocus (Scherzer defocus is even only about -5 nm, which was targeted as imaging setting). The major impact originates from the wavelength and spatial frequency. All values for the image acquisitions in this work are provided below yielding a delocalisation value of approximately -0.06 nm, which is far below the spacings that are interpreted in Fig. S8 and Figs. 3 and 4 in the main text. Note that delocalisation with these settings would grow in absolute value to ca. -0.25 nm for a spatial frequency of 2 nm^{-1}, i.e. for spacings of 0.5 nm.

$\Delta R = \lambda f d + \lambda^3 f^3 C_s$ **Eq. S1**[4]

Variable	Explanation	Value
λ	Electron wavelength corresponding to 200 keV	0.0025 nm
f	Spatial frequency	0.5 nm^{-1}
d	Focus/Defocus	-50 nm
C_s	Spherical aberration	10 µm
ΔR	**Delocalization**	**-0.06 nm**

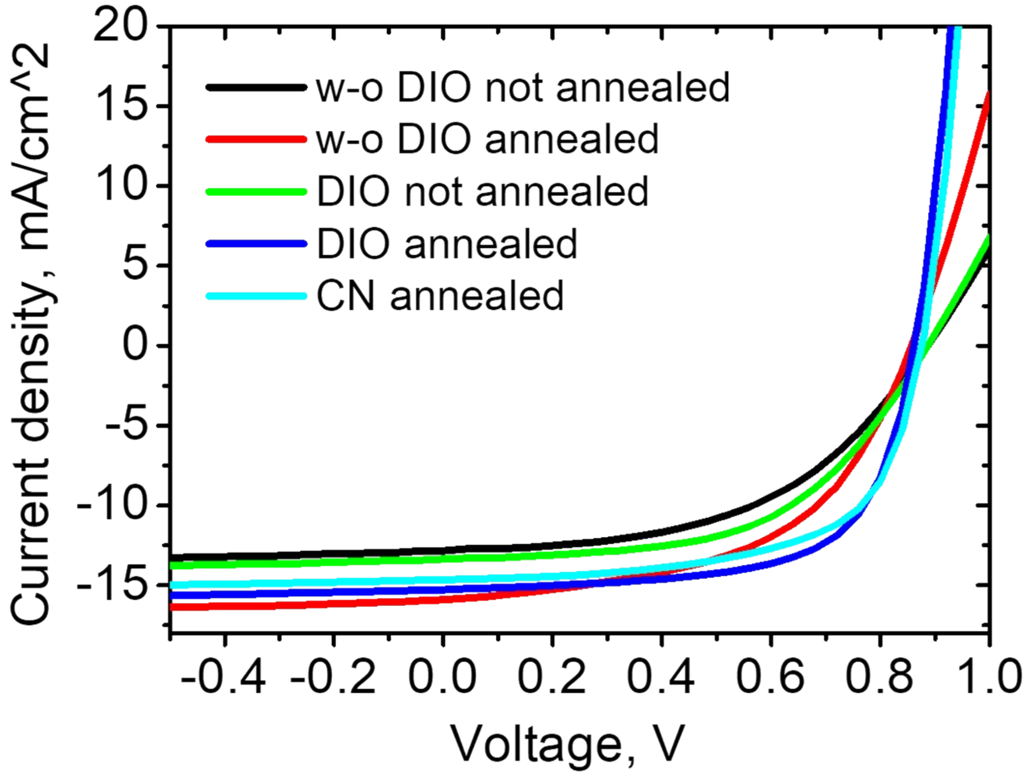

Fig. S9 J-V curves of PBDB-T:ITIC solar cells. The active layers were processed without DIO/CN and with DIO/CN, and exposed or not exposed to the annealing treatment during 15 min at 140 °C.

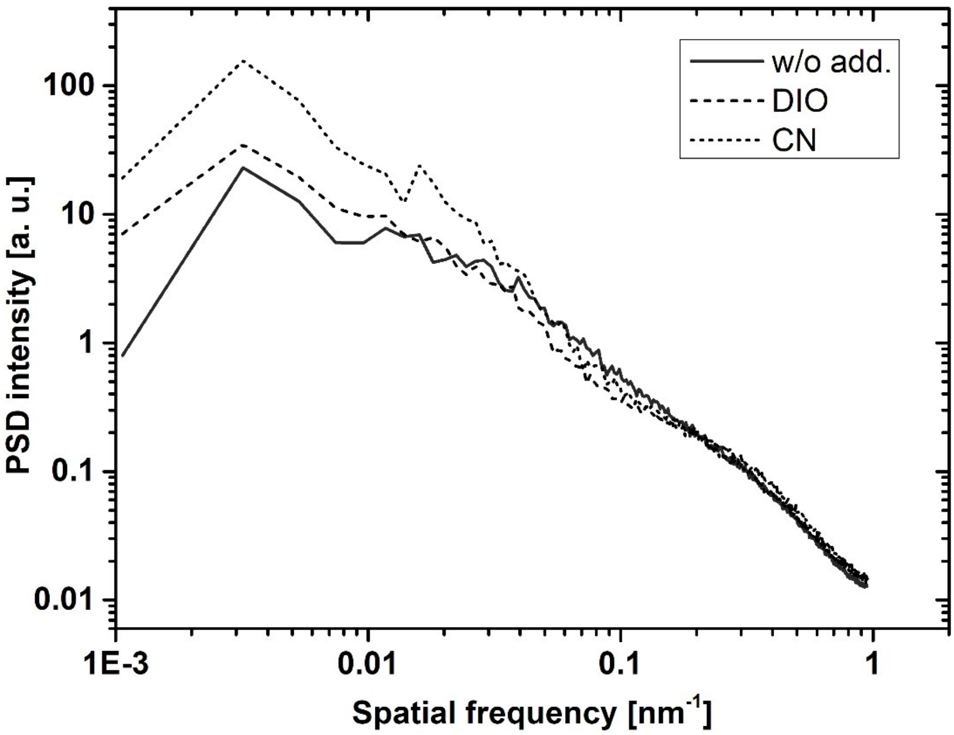

Fig. S10 Power spectral densities (PSDs) for material maps after annealing. The PSDs show radially averaged profiles of the power spectra from the maps shown in Fig. 4a,f,k in the main text. Peaks or shoulders indicate a range of increased occurrences of specific spatial frequencies, i.e. size features in the images. The map for the blend without additive assistance shows a broad shoulder from ca. 0.2-0.015 nm^{-1} corresponding to about 5-67 nm. For layers processed with DIO or CN, the shoulder starts at ca. 0.07 nm^{-1}, reducing the concentration of feature (or domain) sizes to ca. 14-67 nm. For CN, a separate peak appears on this shoulder for corresponding sizes of ca. 33-67 nm. This analysis shows that domain sizes follow a moderate increase with additive assistance for PBDB-T:ITIC.

Table S1 Measurement of the periodic spacings of crystalline donor and acceptor areas from the overlay image in Fig. 3a. The rows show frequencies of occurrences of measured spacings.

phase	**donor**	**acceptor**			
spacing	2.1 nm	1.9 nm	2.0 nm	2.1 nm	2.2 nm
n	6	9	5	3	3

Video S1 Series of an ESI series with inelastic images from 10-39 eV. The inverted contrasts of different phases indicate the nanoscale morphology of a PBDB-T:ITIC blend processed with the additive CN and with thermal annealing at 140 °C for 15 min.

References

1. Han, G., Guo, Y., Song, X., Wang, Y. & Yi, Y. Terminal π–π stacking determines three-dimensional molecular packing and isotropic charge transport in an A–π–A electron acceptor for non-fullerene organic solar cells. *J. Mater. Chem. C* **5**, 4852-4857 (2017).
2. Egerton, R. F. Control of radiation damage in the TEM. *Ultramicroscopy* **127**, 100-108 (2013).
3. Egerton, R. F. *Electron Energy-Loss Spectroscopy in the Electron Microscope*. 3. edn, (Springer, 2011).
4. Williams, D. B. & Carter, C. B. *Transmission Electron Microscopy: A Textbook for Materials Science*. 2 edn, (Springer US, 2009).